



**Remarkable variability of dyke features at the Vicuña Pampa Volcanic Complex, Southern Central Andes**

Journal:	<i>Terra Nova</i>
Manuscript ID	TER-2016-0055.R2
Wiley - Manuscript type:	Paper
Date Submitted by the Author:	n/a
Complete List of Authors:	Guzman, Silvina; CONICET, Instituto de Bio y Geociencias del NOA; Instituto de Ciencias de la Tierra Jaume Almera, Neri, Marco; Istituto Nazionale di Geofisica e Vulcanologia Sezione di Catania Carniel, Roberto; Universita degli Studi di Udine, DPIA Marti, Joan; CSIC, Institute of Earth Sciences 'Jaume Almera' Grosse, Pablo; La Fundacion Miguel Lillo Montero-López, Carolina; CONICET, Instituto de Bio y Geociencias del NOA Geyer, Adelina; Institute of Earth Sciences Jaume Almera, ICTJA-CSIC, Group of Volcanology, SIMGEO (UB-CSIC)
Keywords:	dyke textures, Vicuña Pampa, Central Andes, dykes, volcanic massif

Remarkable variability of dyke features at the Vicuña Pampa  
Volcanic Complex, Southern Central Andes

Silvina Guzmán<sup>1,2</sup>, Marco Neri<sup>3</sup>, Roberto Carniel<sup>4</sup>, Joan Martí<sup>2, a</sup>, Pablo Grosse<sup>5</sup>, Carolina  
Montero-López<sup>1</sup>, Adelina Geyer<sup>2</sup>

<sup>1</sup> Instituto de Bio y Geociencias del NOA (IBIGEO), UNSa, CONICET, 9 de Julio 14, 4405,  
Rosario de Lerma, Salta, Argentina

<sup>2</sup> Institute of Earth Sciences Jaume Almera, ICTJA-CSIC, Lluís Solé i Sabarís s/n, 08028 Barcelona,  
Spain

<sup>3</sup> Istituto Nazionale di Geofisica e Vulcanologia, Osservatorio Etneo-Sezione di Catania, Piazza  
Roma, 2 – 95123 Catania, Italy

<sup>4</sup> Laboratorio di misure e trattamento dei segnali, Dipartimento Politecnico di Ingegneria e  
Architettura (DPIA) Università di Udine, Via delle Scienze, 206 - 33100 Udine, Friuli, Italy

<sup>5</sup> CONICET and Fundación Miguel Lillo, Miguel Lillo 251, 4000 Tucumán, Argentina

<sup>a</sup> Now at the Institut des Sciences de la Terre d'Orléans (ISTO, CNRS), Université d'Orléans,  
Campus Géosciences, 1A rue de la Férolerie, F45071, Orléans Cedex 2, France

Corresponding Author

Silvina Guzmán

Permanent address: Instituto de Bio y Geociencias del NOA (IBIGEO), CONICET-UNSa, 9 de  
Julio 14 (4405), Rosario de Lerma, Salta, Argentina, sguzman@conicet.gov.ar

Tel: +54 387 4931755

Short title: Remarkable variability of dyke features

**Abstract**

Dykes at the Vicuña Pampa Volcanic Complex, mostly basaltic (trachy)-andesite and (trachy)-andesite, are exposed at the base and along the walls of a large depression resulting from intense degradation. Dykes intruding stiff layers (lavas, plugs and necks) are thin, mostly dip  $>60^\circ$  and have coherent textures, whereas dykes intruding more compliant materials (breccias and conglomerates) tend to be thicker, have lower dips and have coherent, brecciated or mixed textures (coherent and brecciated textural domains in a single or compound dyke). Single dykes with brecciated and mixed textures are only found intruding near-surface units. Dykes with mixed textures always have sharp contacts between domains. Dykes with sinuous domain contacts and enclaves of one domain inside the other are interpreted as resulting from dyke arrest, partial cooling, and reinjection of new magma. Dykes with straight domain contacts are considered compound dykes, with a new dyke intruding along the margins of an older, solidified one.

Keywords: dykes, dyke textures, volcanic massif, Vicuña Pampa, Central Andes

**Introduction**

In recent decades, several studies have investigated dyke propagation by focusing on their field characteristics or following a modelling approach (experimental, numerical, analytical and/or analogue). Many of these studies analyze the influence on dyke emplacement of the physical parameters of both host rock and intruding magma. Dyke thickness is highly dependent on the local stresses along the potential dyke path (load of the volcanic edifice above the dyke, depth and distance from the edifice; e.g. Pinel and Jaupart, 2000) and on the stiffness (Young's modulus "E") of the medium they traverse, with thicker dykes found

45 in more compliant host rocks (e.g. Gudmundsson *et al.*, 2012; Delcamp *et al.*, 2012; Geshi  
46 and Neri, 2014). Dyke dip is also found to be deflected or arrested at the contact between  
47 layers (Gudmundsson, 2011; Browning and Gudmundsson, 2015). When crossing layers of  
48 similar stiffness, or when the upper layer is more compliant, the dyke changes from more to  
49 less vertical; however, when the upper layer is stiffer, the dyke tends to be deflected to form  
50 a sill (Gudmundsson, 2011). Although there are several studies focusing on the field  
51 characteristics of dykes (e.g. Ferrari *et al.*, 1991; Gautneb and Gudmundsson, 1992;  
52 Gudmundsson, 1995; Gudmundsson and Brenner, 2005; Goto *et al.*, 2008; Kavanagh and  
53 Sparks, 2011; Delcamp *et al.*, 2012; Daniels *et al.*, 2012; Gudmundsson *et al.*, 2012;  
54 Petronis *et al.*, 2013; Geshi and Oikawa, 2014; Geshi and Neri, 2014; Vezzoli and  
55 Corazzato, 2016), most are focused on their geometrical features, whereas their textural  
56 patterns have received much less attention (e.g. Ferrari *et al.*, 1991; Gautneb and  
57 Gudmundsson, 1992; Goto *et al.*, 2008; Gudmundsson *et al.*, 2012; Petronis *et al.*, 2013;  
58 Geshi and Oikawa, 2014; Geshi and Neri, 2014; Vezzoli and Corazzato, 2016). However,  
59 textures can provide information on the dyke's emplacement history. They can inform on  
60 the rheological, mechanical and/or thermal contrasts between the intruding magma and the  
61 host rock (magma viscosity, crystal segregation, magma rheology, host rock mechanical  
62 properties, local stress fields, depth of emplacement, differences in temperature between  
63 magma and host rock), as well as on whether dykes were single or compound. This is why,  
64 in addition to their geometrical characteristics, textural aspects of dykes need also to be  
65 considered in studies with the aim of understanding the evolution of intrusive episodes in  
66 volcanoes.



Here, we describe the dykes cropping out at the Vicuña Pampa Volcanic Complex (VPVC), southern Central Andes. The geometrical characteristics of these dykes seem to be related to the mechanical properties of the material they intrude, but most importantly they offer a unique case study where in a single volcanic complex there are dykes with purely brecciated textures, purely coherent textures and with both textural domains.

### **Geology of the Vicuña Pampa Volcanic Complex**

The Miocene Vicuña Pampa Volcanic Complex (VPVC), located at the SE margin of the Altiplano-Puna plateau (Fig. 1) and originally considered a collapse caldera (Rossello, 1980; Rossello and Jones, 1999; Viramonte and Petrinovic, 1999), was recently interpreted as a 30-km wide broad volcanic massif that suffered intense degradation (Guzmán *et al.*, 2017).

The first volcanic cycle of the VPVC lies on top of an igneous-metamorphic basement and is formed by plugs and necks (Root Complex; 12.41 Ma), lava flows (Lower Lava Flows Succession and Upper Lava Flows Succession; 12.19 Ma) separated by a thick epiclastic succession (Cerro Morado Epiclastic Succession), block and ash flow deposits (La Cumbre Breccia) and volcanic breccias (Nacimientos Breccia) whose composition mainly ranges from basaltic andesite to andesite (Guzmán *et al.*, 2017). After this first volcanic cycle, the VPVC underwent intense degradation during middle to late Miocene that gave rise to a large morphological depression, 13 to 18 km wide and 1,200 m deep (Guzmán *et al.*, 2017) (Fig. 1). The different units of the first volcanic cycle are exposed on the floor and along the walls of the depression (Fig. 1). The second volcanic cycle occurred after the main degradation of the complex, possibly during the late Miocene, and consists in block and ash

deposits of the Cerro Bayo Breccia, cropping out on the SW floor of the depression (Fig. 1; Guzman *et al.*, 2017).

### **The VPVC dykes**

The VPVC units are cut by hundreds of dyke segments (Guzmán *et al.*, 2017; Carniel *et al.*, 2017) (Fig. 2). These dykes have different characteristics depending on the relative stiffness (Young's modulus  $E$  not measured, but qualitatively estimated) of the material they intrude: the stiffer Root Complex (see Fig. 2, 3 A), or the more compliant Cerro Bayo Breccia (see Fig. 2, 3 B), Nacimientos Breccia and undifferentiated epiclastic/volcanic material. Dykes vary in composition from basaltic (trachy)-andesites to (trachy)-andesites, with only one sampled dyke having dacite composition (see Fig. 4 and Supplementary File 1). Dykes and other magmatic sheet intrusions are most abundant in the western portion of the depression (Fig. 2). During fieldwork we studied 33 dykes, 15 of which were sampled, recording their geographic and stratigraphic position, textures, strike, dip and thickness (Table 1 of Supplementary File 1). More than 85% of the dykes have dip angles ranging from  $60^\circ$  to  $90^\circ$  (see Table 1 of Supplementary File 1), but moderate to low-angle ( $<60^\circ$ ) inclined sheets are also present. Their thickness (field measurements) ranges from 0.4 m to 6 m, with an average of 1 m; their segment lengths (satellite image-based analysis) vary from 12 m to 870 m, with an average of 175 m.

### **Textural characteristics of the VPVC dykes**

Dykes have coherent or brecciated textures, or mixtures of both. Dykes with coherent textures are mainly porphyritic and less commonly aphanitic. They have sharp contacts with the intruded rocks, without the development of glassy or quenched margins, and vary

111 in thickness from 0.4 m to 6 m, and in dip between 35° and 88°. Porphyritic dykes are  
112 plagioclase-phyric and less frequently amphibole-phyric with cm-sized phenocrysts set in  
113 an aphanitic groundmass (Fig. 3 C). Petrographically, coherent dykes show hyalocrystalline  
114 to holocrystalline inequigranular and seriate textures set in a microcrystalline (Fig. 3 D),  
115 cryptocrystalline or vitric groundmass. They are basaltic (trachy)-andesite (see  
116 Supplementary File 1) and contain phenocrysts of plagioclase, clinopyroxene,  
117 orthopyroxene ± amphibole and olivine.

118 Dykes with brecciated textures are characterised by subangular clasts with porphyritic to  
119 aphyric textures in a matrix of the same composition (Fig. 3 E, F). The clasts are  
120 trachyandesitic (phenocrysts of plagioclase, clinopyroxene, orthopyroxene ± amphibole) to  
121 dacitic with hyalocrystalline, seriate textures set in a cryptocrystalline groundmass, where  
122 minerals are smaller and frequently broken (Fig. 3 F). These dykes vary in thickness from 1  
123 m to 3 m and also show sharp contacts with the rocks they intrude. They dip between 38° to  
124 79°.

125 Combinations of brecciated and coherent textural domains are sometimes found in a single  
126 or compound dyke. These mixed textures within dykes always have sharp contacts between  
127 the brecciated margins and the coherent cores or vice versa. Sometimes the contacts are  
128 sinuous (Fig. 3 G, H) and one texture develops as enclaves within the other (Fig. 3 G); in  
129 other cases the contacts are sharp but straight.

130 Dyke - host rock- thickness-texture-composition relationships

131 We can distinguish three groups of dykes according to their geochemical signatures (see  
132 Supplementary File 1 and groups A, B and C in Fig. 4). Small compositional variations

133 within each group may be explained by simple processes such as different crystallization  
134 degrees. Even though the geochemical dataset is limited (9 analyses) we cannot distinguish  
135 dykes according to their textures (Fig. 5 A), mechanical properties of the host-rock (Fig. 5  
136 B), thickness (Fig. 5 C), or dyke dip (Fig. 5 D) as a function of their geochemical  
137 compositions.

138 We have no clear constraints on the possible variability of dyke emplacement depths, but  
139 by combining the stratigraphic relations between dykes and host rocks with geochemical  
140 analysis, we can suggest relative ages of emplacement. Since the Cerro Bayo Breccia was  
141 formed after the central depression and contains feeder dykes (Fig. 3B and 4), we infer that  
142 dykes from groups A and B (i.e. dykes intruding this and other units) are the youngest,  
143 were intruded at shallow levels (fairly close to the original topographic surface) and  
144 therefore suffered negligible erosion during arid conditions (see Guzmán *et al.*, 2017). On  
145 the contrary, the only group of dykes not intruding the Cerro Bayo Breccia (group C; see  
146 Fig. 4 and Supplementary Files) may possibly have been intensely eroded after  
147 emplacement.

148 22 dykes intrude relatively compliant material, consisting of breccias and conglomerates.  
149 Their average thickness is 1.15 m and varies between 0.4 and 6 m (Fig. 6 A), with 75% of  
150 the dykes being thinner than 3 m. They dip between 35° and 90°, with 72% of them having  
151 dip angles greater than 70° (Fig. 6 B). These dykes have coherent, brecciated and mixed  
152 textures with both brecciated domains in the centre or in the borders of coherent ones  
153 within a single or compound dyke (see Fig. 6 C and Table 1 of Supplementary File 1).

11 dykes cut the stiffer Root Complex; their average thickness is 0.6 m and ranges between 0.5 and 2 m, with more than 80% thinner than 1 m (Fig. 6 A). Their dip varies between 60° and 90°, of which 64% dip more than 70° (Fig. 6 B). We recognised only coherent textures (Fig. 6 C), of which more than 80% are porphyritic.

## Discussion

The modest geochemical and mineralogical variability observed among the VPVC dykes indicates that their differences in geometry and textures cannot be attributed to contrasts in magma composition. It seems that dyke thicknesses are - at least partially - controlled by the stiffness of the intruded rocks (Fig. 7), as thicker dykes are found only cutting the relatively more compliant breccias (typical stiffness of 1-10 GPa: Gudmundsson, 2006, 2011; Gudmundsson *et al.*, 2012), while thinner dykes cut both more compliant and stiffer volcanic sequences (typical stiffness up to 100 GPa: Gudmundsson, 2006, 2011; Gudmundsson *et al.*, 2012). This relation matches fully the results obtained by models and previous field studies (see Keating *et al.*, 2008; Geshi *et al.*, 2010, 2012; Gudmundsson *et al.*, 2012; Geshi and Neri, 2014; Rivalta *et al.*, 2013, 2015). However, we found no dykes intruding layers with different stiffness. Furthermore, we do not have constraints on possible differences in the local stress field and/or the load of a volcanic edifice for the different host rocks.

Dykes cutting more compliant materials show shallow dips, whereas those intruding stiffer material always dip >60° (Fig. 6B and 7). The occurrence of shallow dips may be related to dykes intruding near surface units (e.g. Geshi *et al.*, 2010, 2012).

175 The brecciated nature of dykes has previously been explained as due to mechanical erosion  
176 processes - such as particle collision and wall collapse - or as related to phreato-magmatic  
177 or, more generally, to an explosively-driven origin (e.g. Geshi and Neri, 2014, and  
178 references therein; Vezzoli and Corazzato, 2016). Other studies show dykes with bulging  
179 and lobate margins when intruding brecciated host rocks and resulting from magma  
180 propagation along a self-induced shear fault (e.g. Mathius *et al.*, 2008; Petronis *et al.*,  
181 2013); in these cases a mix of dyke breccia and crushed host rock is observed (Petronis *et*  
182 *al.*, 2013). We discuss here a possible explanation for the brecciated and mixed textures,  
183 based mainly on the contact relationships of domains and on their occurrence only near the  
184 surface. At the VPVC, the sharp contacts between dykes with brecciated domains and the  
185 host rock, the similar composition of clasts and matrix and the absence of pumice  
186 fragments or glass shards within the brecciated domains, all seem to indicate a non-  
187 explosive origin, with a fracture mechanism similar to the one proposed by Tuffen *et al.*  
188 (2003) for tuffisites. Therefore, we invoke the possibility of brecciation during a pulsating  
189 emplacement. A sketch illustrating the different stages is presented in figure 8. This  
190 mechanism is somehow similar to that proposed by Geshi and Oikawa (2014) for the  
191 propagation of a dyke near the topographic surface, involving at a first stage materials from  
192 wall rock erosion and collapse. These dykes may be subject to temporary arrests as a  
193 response to a pressure drop when approaching the surface, causing a decrease in their  
194 temperature which, also helped by the exsolution of volatiles (Lister and Kerr, 1991), leads  
195 to drastic changes in their rheology. This can be followed by the arrival of a successive  
196 pulse of magma that in turn may induce fragmentation of the already almost cooled first  
197 magma batch by exceeding its failure strength. In this case, we may see a cross section of  
198 the dyke with a brecciated portion (1<sup>st</sup> magma batch) and a remaining coherent domain (2<sup>nd</sup>

magma batch; see Fig. 8 A). Sometimes, usually closer to the topographic surface, the entire cross section of the dyke may be brecciated (see Fig. 8 B). The time span between the emplacement of the first magma batch in the dyke and the arrival of the second batch was very short ( $\sim 4.6$  days for a 1 m thick dyke; see estimations in the Supplementary File 2), as the sharp and sinuous contacts and the presence of enclaves of one textural domain within the other are evidence of a ductile deformation. The few cases in which the brecciated domain is in the central portion of the dyke, and the contacts between the domains are straight, may be explained by the intrusion of a second dyke in the same place where a formerly emplaced pulsating dyke was already totally solidified (Fig. 9). The new dyke uses the previous weakness zone to intrude, passing between the margins of the former dyke and the host-rock, thus becoming a compound dyke. The resulting scenario shows the original central brecciated dyke enclosed by a second coherent one (Fig. 9 A), with sharp but straight contacts. The proposed mechanism of formation of the brecciated textural domains (when the whole dyke is brecciated or when the brecciated domain is found at the margin of the dyke) indicates near surface conditions.

**Conclusions**

At the Vicuña Pampa Volcanic Complex, dykes with three types of textures - coherent, brecciated and mixed - intrude several units of the complex with different stiffness. Dykes intruding stiffer materials are always coherent and tend to be thinner and more vertical; on the contrary, those cutting more compliant materials are generally thicker, have highly variable dip angles and can have any of the three textures. Vertical to sub-vertical dykes intrude any unit regardless of their stiffness, but inclined sheets ( $<60^\circ$ ) are only present when intruding compliant materials.

The presence of dykes with brecciated and mixed textures is interpreted without the need to invoke explosivity or erosion of the host rock, but as a result of arrest events during dyke propagation/evolution at shallow levels; brecciated textures result when magma re-injection within semi-solidified dyke portions produce their mechanical fragmentation. Compound dykes can be generated when a second dyke intrudes along the margins of a previous solidified dyke.

## Acknowledgements

SG, CML and PG are grateful for funding by ANPCyT (PICT 2012-0419; PICT 2011-0407), CONICET (PIP 489, PIP 286) and CIUNSa 1810. JM is grateful for the MECD (PRX16/00056) grant. AG is grateful for her Ramón y Cajal contract (RYC-2012-11024). S. Conway is thanked for improving the English. We acknowledge the very constructive revisions made by Drs. John Browning and Thierry Menand and suggestions by the editors, Drs. Jean Braun and Agust Gudmundsson.

## References

- Carniel, R., Guzmán, S. and Neri, M., 2017. FIERCE: FInding volcanic ERuptive CEnters by a grid-searching algorithm in R. *Bulletin of Volcanology*, **79**:19, doi: 10.1007/s00445-017-1102-3
- Browning, J. and Gudmundsson, A., 2015. Caldera faults capture and deflect inclined sheets: an alternative mechanism of ring dike formation. *Bulletin of Volcanology*, **77**:4, doi: 10.1007/s00445-014-0889-4



243 Daniels, K A., Kavanagh, J.L., Menand, T. and Sparks, S. J., 2012. The shapes of dikes:  
 244 Evidence for the influence of cooling and inelastic deformation. *GSA Bulletin*, **124**, (7/8),  
 245 1102–1112, doi: 10.1130/B30537.1

246 Delcamp, A., Troll, V. R., van Wyk de Vries, B., Carracedo, J. C., Petronis, M. S., Pérez-  
 247 Torrado, F. J. and Deegan, F. M., 2012. Dykes and structures of the NE rift of Tenerife,  
 248 Canary Islands: a record of stabilisation and destabilisation of ocean island rift zones  
 249 *Bulletin of Volcanology*, **74**, 963-980.

250 Ferrari, L., Garduño, V.H. and Neri, M., 1991. I dicchi della Valle del Bove, Etna: un  
 251 metodo per stimare le dilatazioni di un apparato vulcanico *Mem. Soc. Geol. It*, **47**, 495-508.

252 Gautneb, H. and Gudmundsson, A., 1992. Effect of local and regional stress fields on sheet  
 253 emplacement in West Iceland. *Journal of Volcanology and Geothermal Research*, **51**, 339-  
 254 356.

255 Geshi, N., Kusumoto, S. and Gudmundsson, A., 2010. The geometric difference between  
 256 non-feeders and feeder dikes *Geology*, **38**, 195-198, doi: 10.1130/G30350.1.

257 Geshi, N., Kusumoto, S., and Gudmundsson, A., 2012. Effects of mechanical layering of  
 258 host rocks on dike growth and arrest *Journal of Volcanology and Geothermal Research*  
 259 **223–224**, 74–82.

260 Geshi, N. and Neri, M., 2014. Dynamic feeder dyke systems in basaltic volcanoes: the  
 261 exceptional example of the 1809 Etna eruption (Italy) *Front. Earth Sci.* **2**:13. doi:  
 262 10.3389/feart.2014.00013.

263 Geshi, N. and Oikawa, T., 2014. The spectrum of basaltic feeder systems from effusive lava  
 264 eruption to explosive eruption at Miyakejima volcano, Japan *Bull. Volcanol.* **76**:797.doi:  
 265 10.1007/s00445-014-0797-7.

- 266 Goto, Y., Nakada, S., Kurokawa, M., Shimano, T., Sugimoto, T., Sakuma, S., Hoshizumi,  
267 H., Yoshimoto and M., Uto; K., 2008. Character and origin of lithofacies in the conduit of  
268 Unzen volcano, Japan. *Journal of Volcanology and Geothermal Research*, **175**, 45–59.
- 269 Gudmundsson, A., 1995. Infrastructure and mechanics of volcanic systems in Iceland.  
270 *Journal of Volcanology and Geothermal Research*, **64**, 1-22.
- 271 Gudmundsson, A., and Brenner, J. S., 2005. On the conditions of sheet injections and  
272 eruptions in stratovolcanoes. *Bull Volcanol*, **67**, 768-782, doi: 10.1007/s00445-005-0433-7
- 273 Gudmundsson, A., 2006. How local stresses control magma-chamber ruptures, dyke  
274 injections, and eruptions in composite volcanoes *Earth Sci. Rev.*, **79**, 1–31.
- 275 Gudmundsson, A., 2011. Deflection of dykes into sills at discontinuities and magma-  
276 chamber formation *Tectonophysics*, **500**, 50-64.
- 277 Gudmundsson, A., Kusumoto, S., Simmenes, T.H., Philipp, S.L., Larsen, B. and Lotveit,  
278 I.F., 2012. Effects of overpressure variations on fracture apertures and fluid transport.  
279 *Tectonophysics*, **581**, 220–230. doi:10.1016/j.tecto.2012.05.003.
- 280 Guzmán, S., Strecker, M.R., Martí J, Petrinovic, I., Schildgen, T.F., Grosse, P, Montero-  
281 López, C., Neri, M., Carniel, R., Hongn, F.D., Muruaga, C. and Sudo, M., 2017.  
282 Construction and degradation of a broad volcanic massif: the Vicuña Pampa volcanic  
283 complex, southern Central Andes, NW Argentina. *GSA Bulletin*, in press.  
284 doi:10.1130/B31631.1
- 285 Kavanagh, J., and Sparks, R.S.J., 2011. Insights of dyke emplacement mechanics from  
286 detailed 3D dyke thickness datasets. *Journal of the Geological Society of London*, **168**,  
287 965–978, doi:10.1144/0016-76492010-137.

288 Keating, G.N., Valentine, G.A., Krier, D.J. and Perry, F.V., 2008. Shallow plumbing  
289 system for small-volume basaltic volcanoes *Bull. Volcanol.*, **70**, 563-582. doi:  
290 10.1007/s00445-007-0154-1.

291 Le Maitre, R., Bateman, P., Dudek, A., Keller, J., Lameyre Le Bas, M., Sabine, P.,  
292 Schmid, R., Sorensen, H., Streckeisen, A., Woolley, A. and Zanettin, B., 1989. A  
293 classification of igneous rocks and glossary of Terms. Blackwell, Oxford.

294 Lister, J.R. and Kerr, R.C., 1991. Fluid-mechanical models of crack propagation and their  
295 application to magma transport in dykes *J. Geophys. Res.*, **96**, 10049-10077.

296 Mathieu, L., van Wyk de Vries, B., Holohan, E.P., Troll, V.R., 2008. Dykes, cups, saucers  
297 and sills: analogue experiments on magma intrusion into brittle rocks. *Earth Planet Sci*  
298 *Lett*, **27**, (1–4), 1–13.

299 McDonough, W.F. and Sun, S., 1995. The composition of the Earth. *Chem. Geol.*, **120**,  
300 223–253.

301 Petronis, M. S., Delcamp, A. and van Wyk de Vries, B., 2013. Magma emplacement into  
302 the Lemptégy scoria cone (Chaîne Des Puys, France) explored with structural, anisotropy  
303 of magnetic susceptibility, and Paleomagnetic data. *Bull Volcanol*, **75**, 753.

304 Pinel, V., and Jaupart, C., 2000. The effect of edifice load on magma ascent beneath a  
305 volcano. *Philosophical Transactions of the Royal Society of London, ser. A, Mathematical*  
306 *and Physical Sciences*, **358**, 1515–1532, doi:10.1098/rsta.2000.0601.

307 Rivalta, E., Böttinger, M., Schnese, M. and Dahm, T., 2013. Supplement to: Buoyancy-  
308 driven fracture ascent: Experiments in layered gelatin.  
309 <http://www.youtube.com/watch?v=8y4U1vrk-gg>

310 Rivalta, E., Taisne, B., Bungler, A. and Katz, R., 2015. A review of mechanical models of  
311 dike propagation: Schools of thought, results and future directions *Tectonophysics*, **638**, 1-  
312 42.

313 Rossello, E. 1980. Nuevo Complejo Volcánico Vicuña Pampa, departamento Belén,  
314 provincia de Catamarca. *Revista de la Asociación Geológica Argentina*, **35** (3), 436-438.

315 Rossello, E.A, and Jones, J.P., 1999. Potencial geominero de la caldera Vicuña Pampa (27°  
316 00'S-67° 00'W), Catamarca, in Proceedings, Congreso Geológico Argentino, 14th, Salta, **2**,  
317 294-297.

318 Tuffen, H., Dingwell, D.B. and Pinkerton, H., 2003. Repeated fracture and healing of silicic  
319 magma generate flow banding and earthquakes? *Geology*, **31**, 1089–1092.

320 Vezzoli, L. and Corazzato, C., 2016. Volcaniclastic dykes tell on fracturing, explosive  
321 eruption and lateral collapse at Stromboli volcano (Italy) *Journal of Volcanology and*  
322 *Geothermal Research*, **318**, 55–72.

323 Viramonte, J.G., and Petrinovic, I.A., 1999. La caldera de Culampajá: una caldera basáltica  
324 en la Puna Austral, in Proceedings, Congreso Geológico Argentino, 14th, Salta, **2**, 235.

325

## 326 **Figure captions**

327 Fig. 1: Geological map of the Vicuña Pampa Volcanic Complex. Modified from Guzman *et*  
328 *al.* (2017).

329 Fig. 2: Dykes distribution within the VPVC, differentiating the units they intrude and their  
330 textures (for the 33 dykes described in the field).

Fig. 3: A) dykes - dotted white lines along margins - intruding the Root Complex (stiff material; note person for scale. B) dykes - dotted white lines along margins - cutting the Cerro Bayo Breccia (relatively compliant material), and a small lava flow above Cerro Bayo Breccia - continuous white line. C) dyke with coherent plagioclase-phyric texture (see dyke 1 in Table 1). D) microphotograph of a dyke with porphyric texture and microcrystalline matrix. E) dyke with brecciated texture (see dyke 8 in Table 1); dashed black lines indicate the borders of some fragments within the breccia. F) microphotograph of a brecciated dyke; dashed yellow lines indicate the borders of some fragments within the breccia. G) dyke with mixed textures (dyke 33 in Table 1); the margin shows a brecciated texture (Br) and displays a sharp-ductile contact (black line) with the coherent (Coh) porphyric inner domain; note (circle) that some portions of the porphyric domain are included in the brecciated domain. H) microphotograph of the dyke in Fig. 3G; brecciated (Br) and coherent (Coh) porphyric texture separated by a sharp and sinuous contact (dashed yellow line).

Fig. 4: A) General sketch of the stratigraphic relations between dykes and host rocks; colours indicate the different geochemical groups of dykes. Note that dykes from groups A and B cut the Cerro Bayo Breccia (CBB; post-depression unit) and other units and those from group C cut the older Root Complex and undifferentiated volcanic/epiclastic deposits (pre-depression units). Vertical prolongation of dykes is represented by dashed lines (black for pre-main degradation intrusions and grey for post-Cerro Bayo Breccia) indicating the possible original location of their tips; B-C) main evidences of discrimination of geochemical groups of dykes; differences in major elements may be related to variable degrees of crystal fractionation B) Total Alkalies Silica diagram (Le Maitre *et al.*, 1989); C)

354 Ba/Th vs Eu/Eu\* diagram, D-F) chondrite-normalised diagrams (Mc Donough and Sun,  
355 1995) of d) dykes from group A, E) dykes from group B; F) dykes from group C.

356 Fig. 5: Harker diagrams of Zr (ppm) vs Sr (ppm) as a function of: A) textures, B) stiffness  
357 of intruded material, C) dyke thickness, D) dyke dip. Colours indicate geochemical groups  
358 as in Fig. 4.

359 Fig. 6: Histograms of dyke thickness (A), dip (B), and textures (C) as a function of host  
360 rock stiffness.

361 Fig. 7: Thickness versus dip of dykes in relation to the stiffness of the units they intrude.

362 Fig. 8: Schematic interpretation of a pulsating dyke;  $t_1$ ,  $t_2$ , and  $t_3$  indicate three stages during  
363 the formation of a single pulsating dyke. In  $t_1$ , the first magma batch is emplaced; in  $t_2$ , the  
364 second magma batch intrudes, producing upward pressure (black arrows) and consequent  
365 fragmentation of the first magma batch;  $t_3$  shows the final result: a coherent core and  
366 brecciated margins separated by sharp and sinuous contacts. A) Portion with brecciated  
367 margin and coherent core; the limit between textural domains is marked by a black line, as  
368 well as small enclaves of the coherent domain inside the brecciated one; some enclaves on  
369 the brecciated domain inside the coherent ones are highlighted in grey. B) Brecciated  
370 portion of a dyke.

371 Fig. 9: Schematic interpretation of a compound dyke formed by an inner pulsating dyke  
372 (see schematic process in Fig. 8) plus an outer single dyke emplaced along the margins;  
373 note the inner brecciated domain is contained and wrapped by the external coherent  
374 domain.

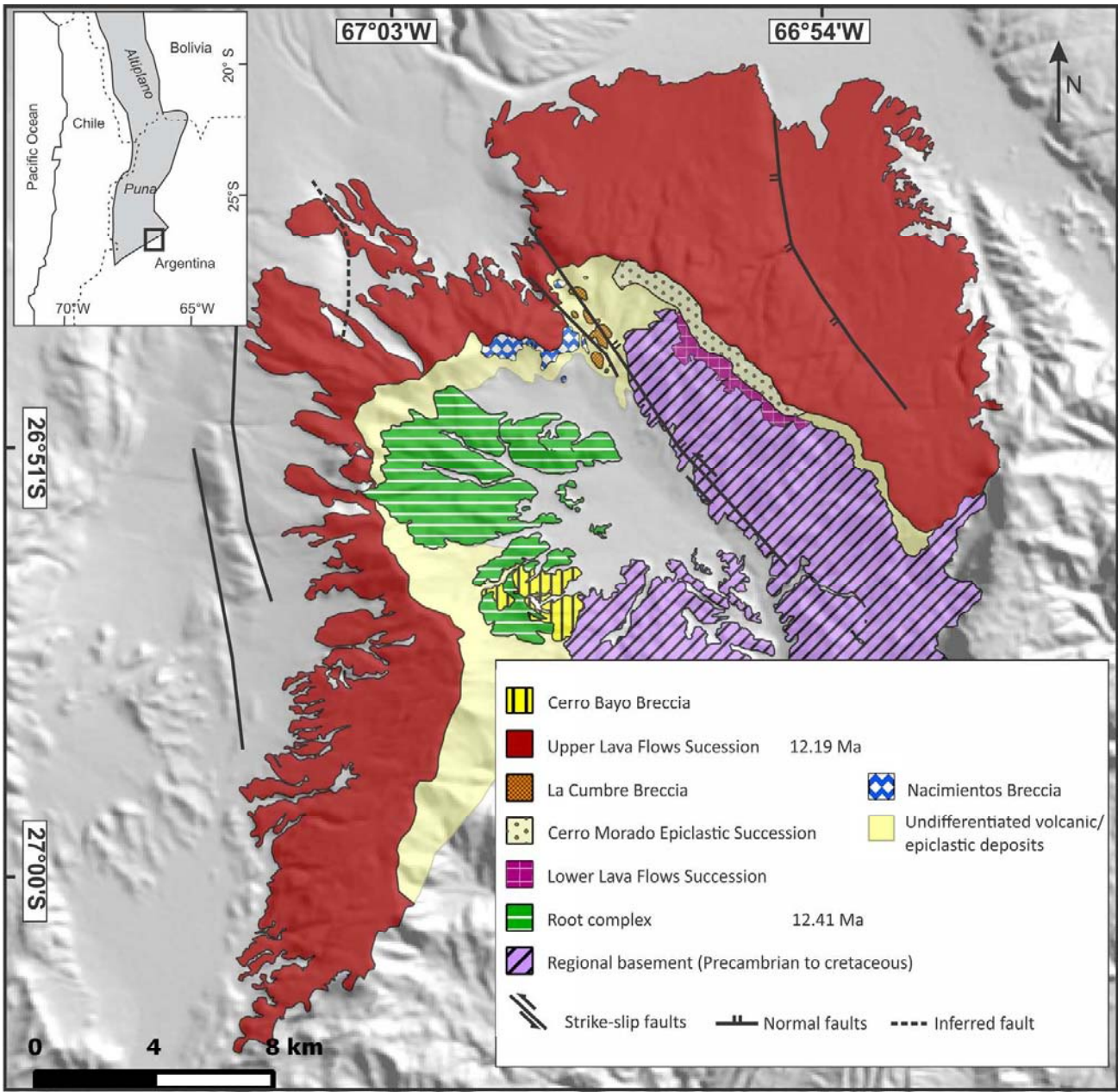


Fig.1

Fig. 1. Geological map of the Vicuña Pampa Volcanic Complex. Modified from Guzman et al. (2017).

173x180mm (300 x 300 DPI)



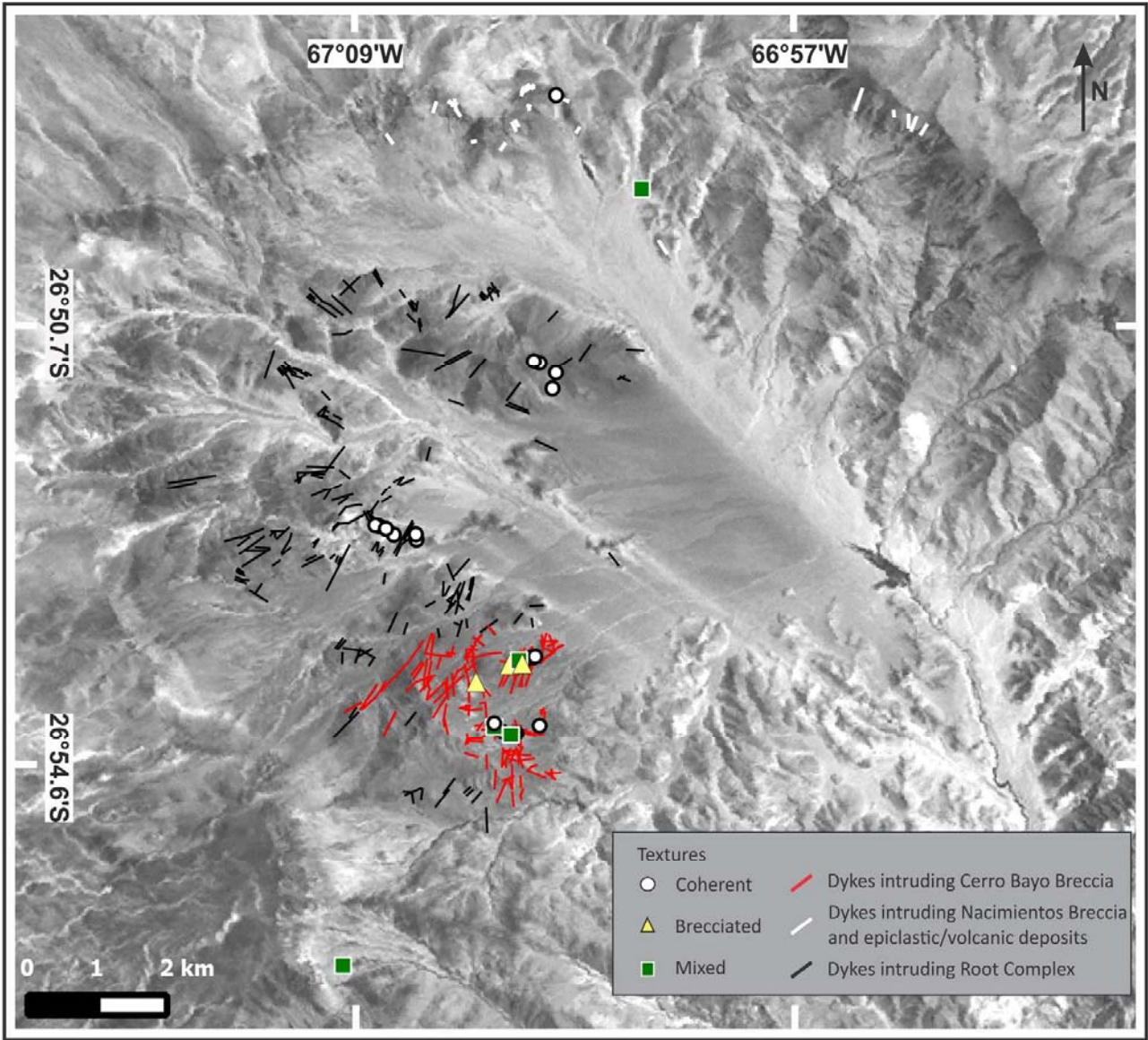


Fig. 2

Fig. 2: Dykes distribution within the VPVC, differentiating their textures and the units they intrude.

155x148mm (300 x 300 DPI)



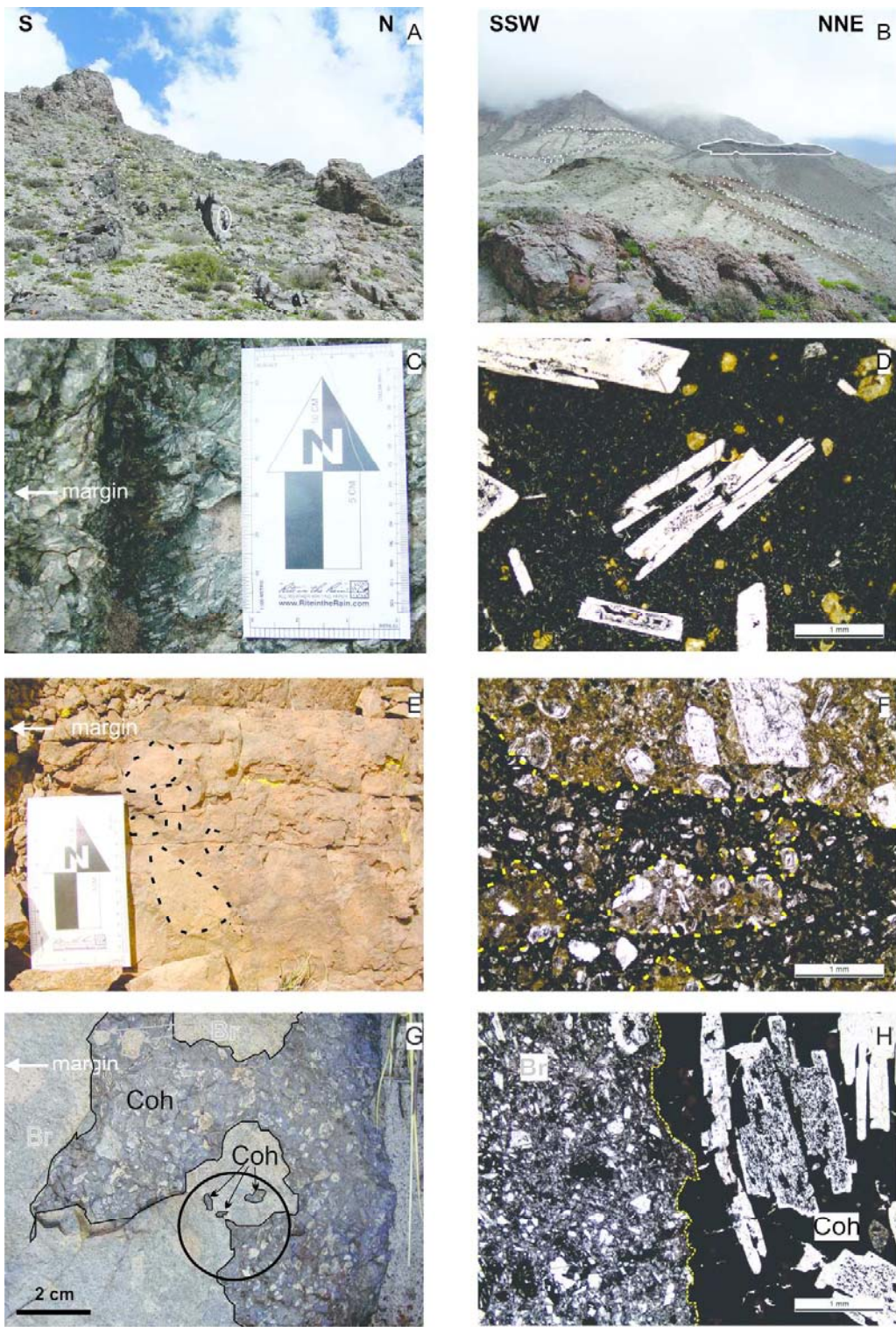


Fig. 3

Fig. 3: A) dykes - dotted white lines along margins - intruding the Root Complex (stiff material; note person for scale. B) dykes - dotted white lines along margins - cutting the Cerro Bayo Breccia (relatively compliant material), and a small lava flow above Cerro Bayo Breccia - continuous white line. C) dyke with coherent plagioclase-phyric texture (see dyke 1 in Table 1). D) microphotograph of a dyke with porphyric texture and microcrystalline matrix. E) dyke with brecciated texture (see dyke 8 in Table 1); dashed black lines indicate the borders of some fragments within the breccia. F) microphotograph of a brecciated dyke; dashed yellow lines indicate the borders of some fragments within the breccia. G) dyke with mixed textures (dyke 33 in Table 1); the margin shows a brecciated texture (Br) and displays a sharp-ductile contact (black line) with the coherent (Coh) porphyric inner domain; note (circle) that some portions of the porphyric domain are included in the brecciated domain. H) microphotograph of the dyke in Fig. 3G; brecciated (Br) and coherent (Coh) porphyric texture separated by a sharp and sinuous contact (dashed yellow line).

145x222mm (300 x 300 DPI)



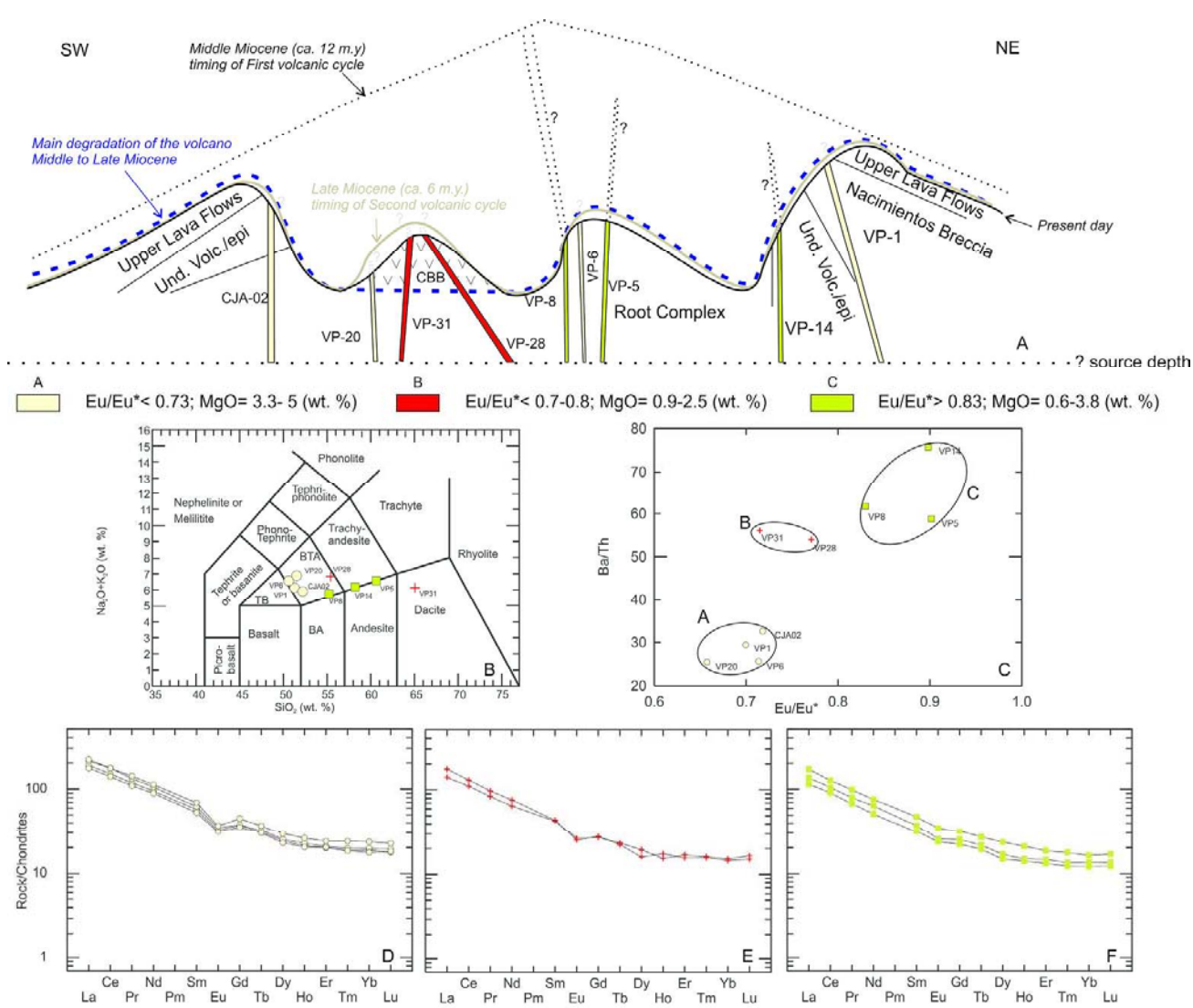


Fig. 4

Fig. 4: A) General sketch of the stratigraphic relations between dykes and host rocks; colours indicate the different geochemical groups of dykes. Note that dykes from groups A and B cut the Cerro Bayo Breccia (CBB; post-depression unit) and other units and those from group C cut the older Root Complex and undifferentiated volcanic/epiclastic deposits (pre-depression units). Vertical prolongation of dykes is represented by dashed lines (black for pre-main degradation intrusions and grey for post-Cerro Bayo Breccia) indicating the possible original location of their tips; B-C) main evidences of discrimination of geochemical groups of dykes; differences in major elements may be related to variable degrees of crystal fractionation B) Total Alkalies Silica diagram (Le Maitre et al., 1989); C) Ba/Th vs Eu/Eu\* diagram, D-F) chondrite-normalised diagrams (Mc Donough and Sun, 1995) of d) dykes from group A, E) dykes from group B; F) dykes from group C.

209x184mm (300 x 300 DPI)



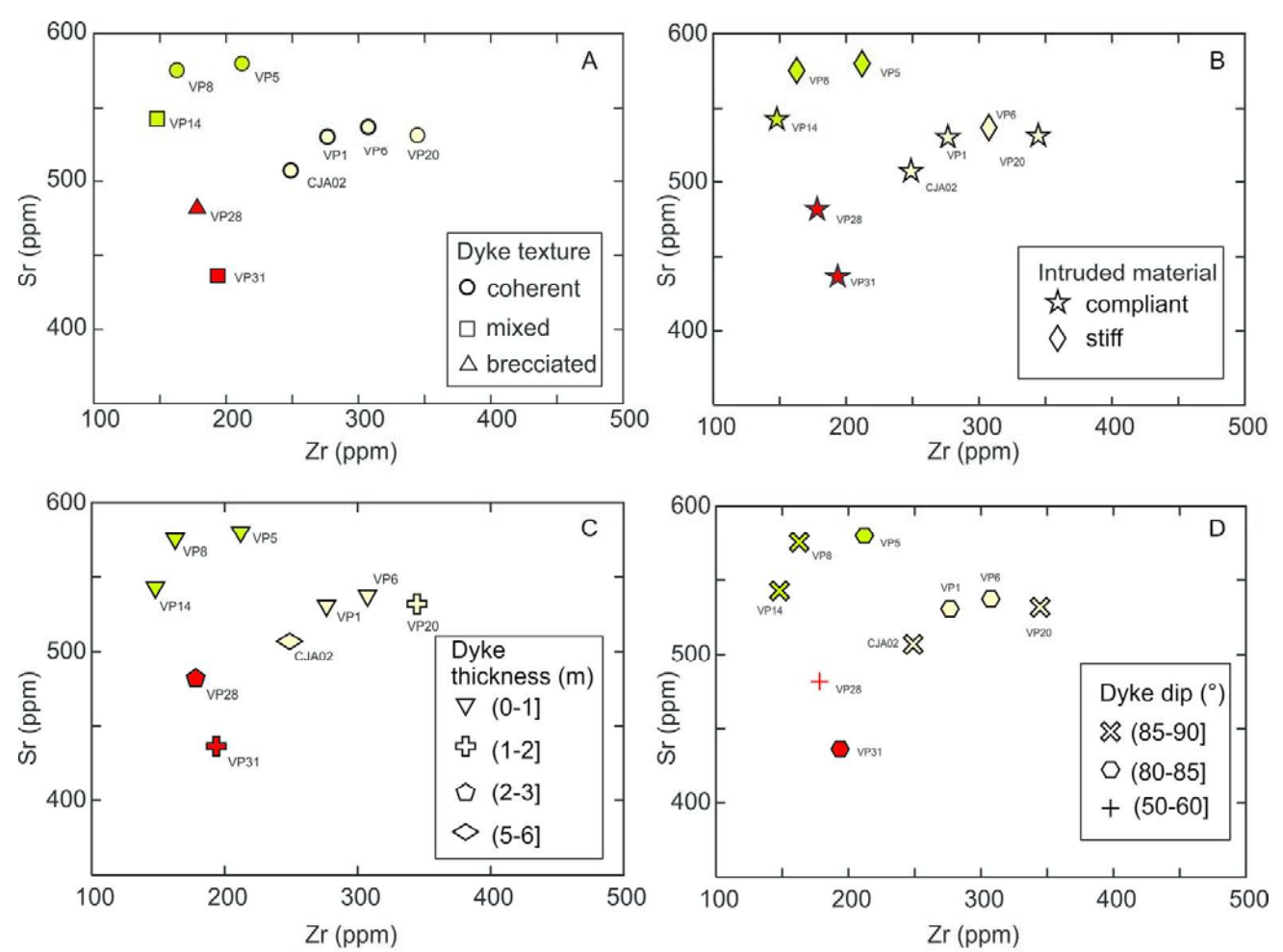


Fig.5

Fig. 5: Harker diagrams of Zr (ppm) vs Sr (ppm) as a function of: A) textures, B) stiffness of intruded material, C) dyke thickness, D) dyke dip. Colours indicate geochemical groups as in Fig. 4.

150x123mm (300 x 300 DPI)

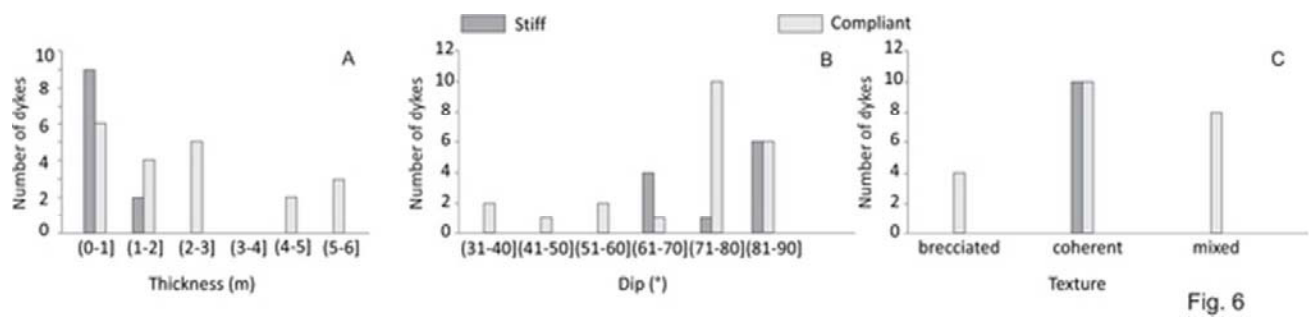


Fig. 6: Histograms of dyke thickness (A), dip (B), and textures (C) as a function of host rock stiffness.

55x12mm (300 x 300 DPI)

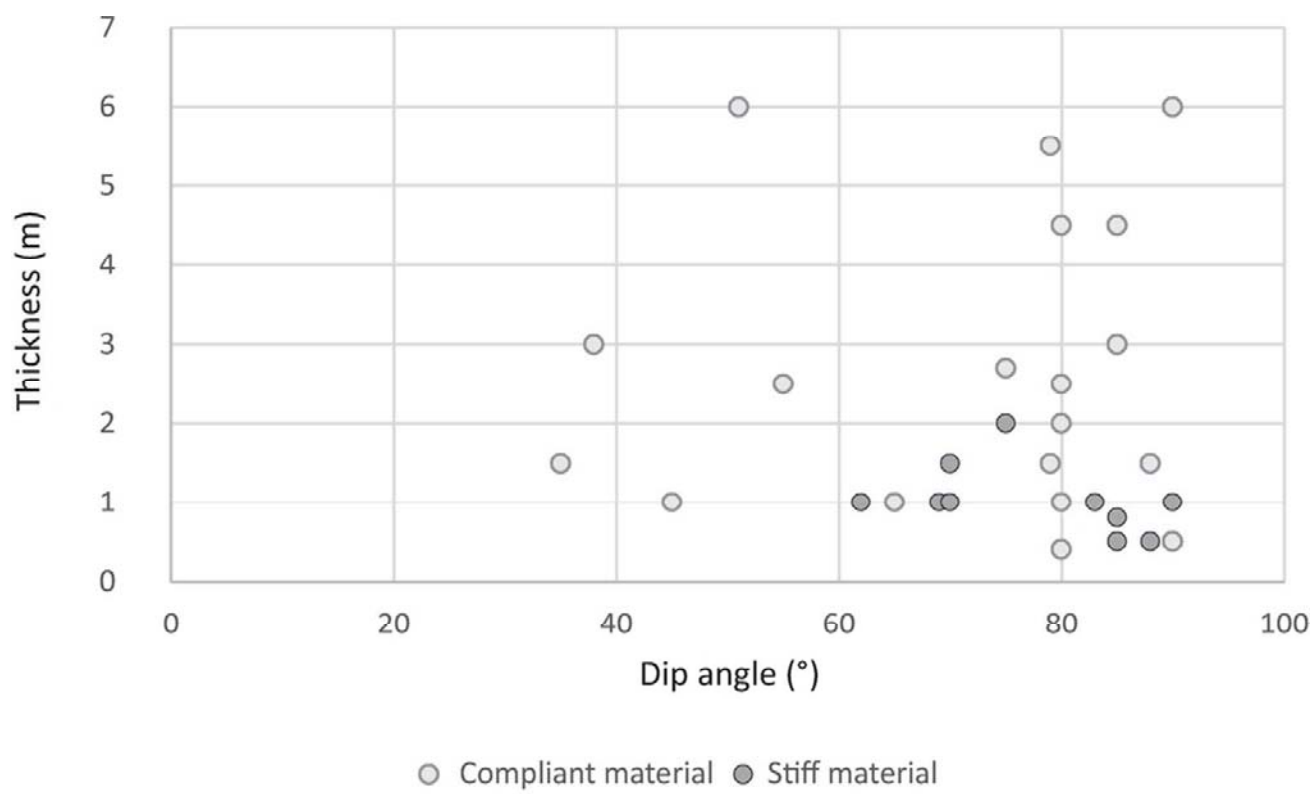


Fig. 7

Fig. 7: Thickness versus dip of dykes in relation to the stiffness of the units they intrude.

82x54mm (300 x 300 DPI)

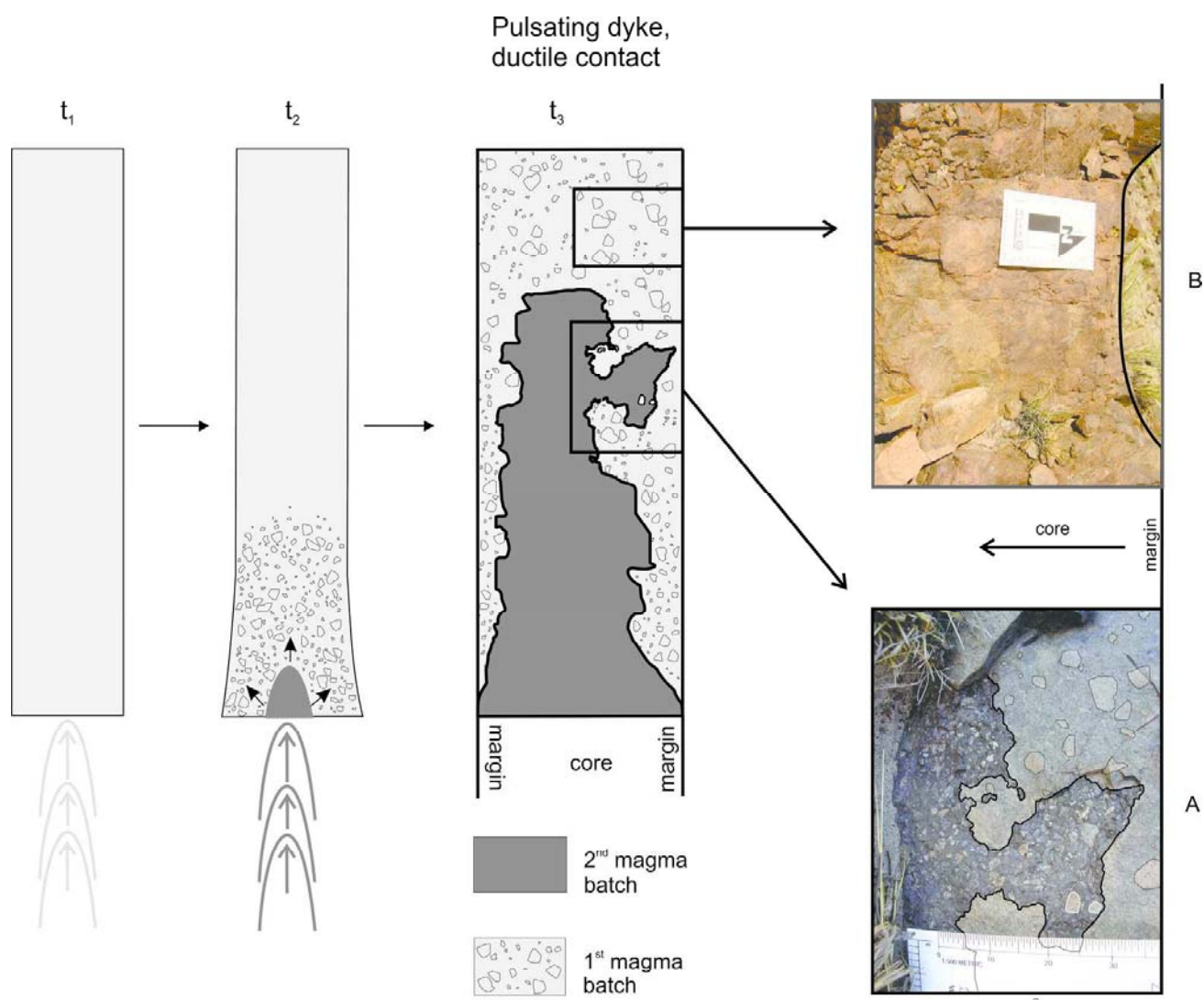


Fig. 8

Fig. 8: Schematic interpretation of a pulsating dyke;  $t_1$ ,  $t_2$ , and  $t_3$  indicate three stages during the formation of a single pulsating dyke. In  $t_1$ , the first magma batch is emplaced; in  $t_2$ , the second magma batch intrudes, producing upward pressure (black arrows) and consequent fragmentation of the first magma batch;  $t_3$  shows the final result: a coherent core and brecciated margins separated by sharp and sinuous contacts. A) Portion with brecciated margin and coherent core; the limit between textural domains is marked by a black line, as well as small enclaves of the coherent domain inside the brecciated one; some enclaves on the brecciated domain inside the coherent ones are highlighted in grey. B) Brecciated portion of a dyke.

172x154mm (300 x 300 DPI)

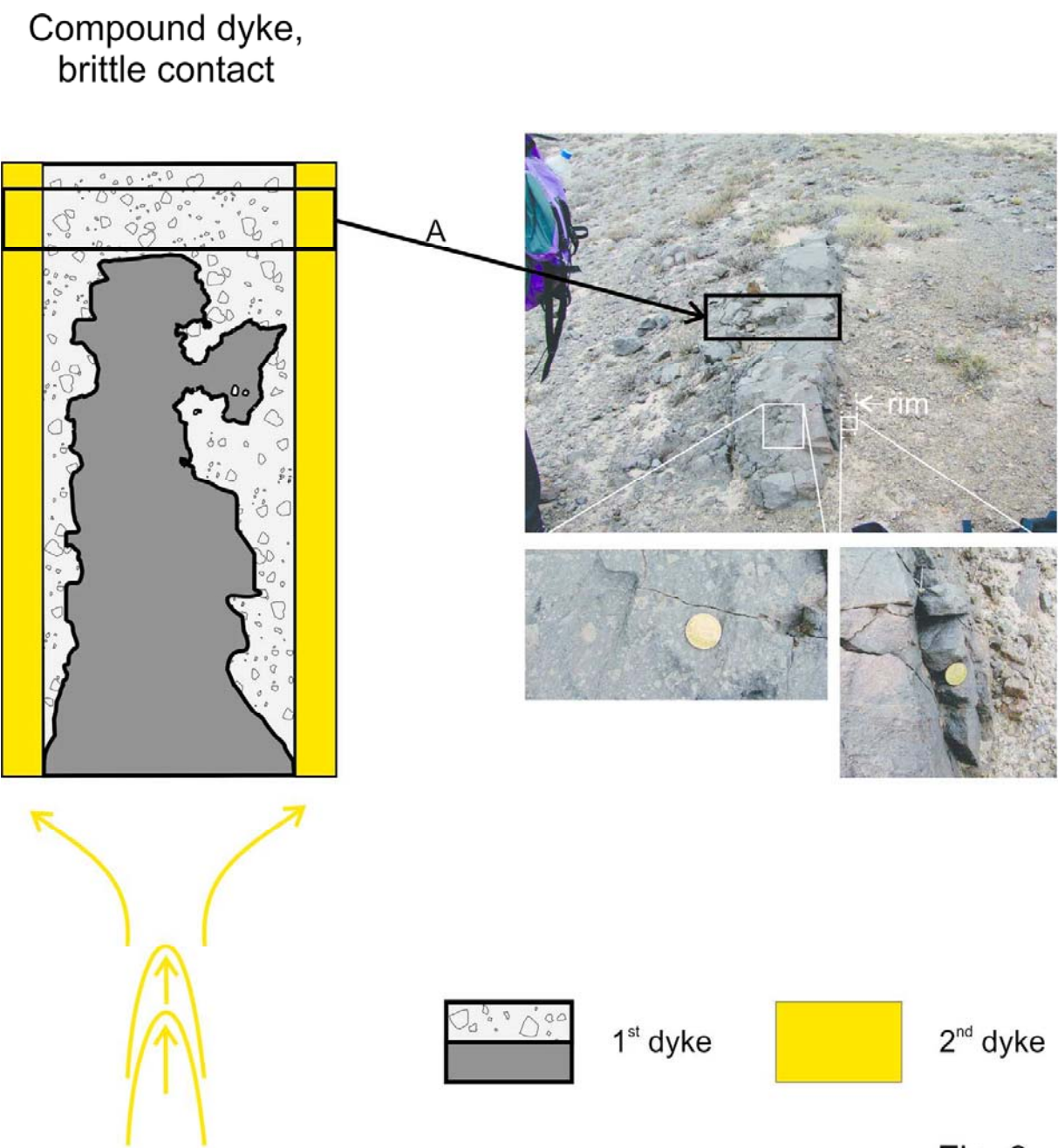


Fig. 9

Fig. 9: Schematic interpretation of a compound dyke formed by an inner pulsating dyke (see schematic process in Fig. 8) plus an outer single dyke emplaced along the margins; note the inner brecciated domain is contained and wrapped by the external coherent domain.

135x139mm (300 x 300 DPI)



Supplementary File 1

Table 1: Dykes location and their main features

Dyke number	Location		Sample	Dip (°)	Strike	Texture	Thickness (m)	Intruded unit
	Latitude (S)	Longitude (W)						
1	26°54'42"	66°59'15"	VP 20	88	269	coherent-P	1.5	Cerro Bayo
2	26°54'41"	66°59'17"		80	330	coherent-P	2.5	Cerro Bayo
3	26°54'40"	66°59'18"	VP 23	85	248	coherent-A	4.5	Cerro Bayo
4	26°54'44"	66°59'21"	VP 24	38	151	brecciated	3	Cerro Bayo
5	26°54'41"	66°59'21"		65	178	coherent-P	1	Cerro Bayo
6	26°54'43"	66°59'25"		75	25	brecciated (m) coherent-P (c)		Cerro Bayo
7	26°54'43"	66°59'25"		77	24	brecciated (m) coherent-P (c)		Cerro Bayo
8	26°54'42"	66°59'28"	VP 25	79	166	brecciated	1.5	Cerro Bayo
9	26°54'47"	66°59'32"		45	340	brecciated	1	Cerro Bayo
10	26°54'54"	67°00'45"	VP 28	55	164	brecciated	2.5	Cerro Bayo
11	26°54'16"	66°59'10"		80	340	coherent-P	4.5	Cerro Bayo
12	26°54'21"	66°59'22"		85	358	coherent-P	3	Cerro Bayo
13	26°54'20"	66°59'24"		80	314	coherent-P	1	Cerro Bayo
14	26°54'22"	66°59'25"	VP-31	80	359	coherent-P (m), brecciated (c)	2	Cerro Bayo
15	26°54'20"	66°59'25"		90	350	coherent-P (m), brecciated (c)	0.5	Cerro Bayo
16	26°54'21"	66°59'27"		79	356	coherent (P)	5.5	Cerro Bayo
17	26°54'21"	66°59'29"		35	44	coherent (P)	1.5	Cerro Bayo
18	26°54'14"	66°59'32"	VP-32	51	69	coherent-A (m), coherent-P (c)	6	Cerro Bayo
19	26°54'18"	66°59'35"		75	352	coherent and brecciated	2.5-3	Cerro Bayo
20	26°53'39"	67°00'15"		62	205	coherent-P	1	Root Complex
21	26°53'37"	67°00'16"		69	236	coherent-P	1	Root Complex
22	26°53'36"	67°00'19"		70	180	coherent-P	1	Root Complex

23	26°53'37"	67°00'27"	VP-40	83	48	coherent-P	1	Root Complex
24	26°53'34"	67°00'31"		75	59	coherent-P	2	Root Complex
25	26°53'33"	67°00'35"		88	76	coherent-P	0.5	Root Complex
26	26°53'33"	67°00'37"		70	192	coherent-P	1.5	Root Complex
27	26°51'21"	66°59'05"	VP8	90	104	coherent-P	1	Root Complex
28	26°51'11"	66°59'02"	VP7	85	70	coherent (A)	0.8	Root Complex
29	26°51'07"	66°59'15"	VP5	85	350	coherent (A)	0.5	Root Complex
30	26°51'07"	66°59'13"	VP6	85	58	coherent (P)	0.5	Root Complex
31	26°49'48"	66°59'03"	VP-1	80	38	coherent (P)	0.4	Nacimientos breccia
32	26°50'36"	66°58'18"	VP-14	90	20	coherent-P (m), brecciated (c),	0.5	undifferentiated volcanic/epiclastic deposits
33	26°56'21"	67°00'54"	CJA-02	90	5	brecciated (m) coherent-P (c)	6	undifferentiated volcanic/epiclastic deposits

P: porphyritic   A: aphanitic   m: margin   c: core

Approaches to relative ages and relative emplacement depth of dykes

The Vicuña Pampa Volcanic Complex has several dykes that vary in composition from basaltic trachyandesite to dacite. Dykes intrude all units of the complex. This 12 My complex was subject to an intense degradation during Middle and Late Miocene, leading to the present depression (Guzmán et al., 2017). No ages for the dykes are known and we can only assess their possible relative ages with respect to the units they intrude. Knowing the relative ages may be helpful to understand the load they were subjected to (because the volcano suffered intense degradation).

Cerro Bayo Breccia, which is considered the youngest unit of the whole complex, possibly of Late Miocene age, crops out within the depression and was formed after the intense degradation. This unit contains dykes that fed small lava flows. Some dykes intruding this unit are eroded to some degree, which we estimate to be very low, owing to the arid climate characterising the eastern Puna plateau since ca. 6 Ma. We thus interpret that all dykes intruding this unit are near the surface and were not subjected to substantial load effects by the volcanic edifice.

Nacimientos Breccia and the undifferentiated volcanic/epiclastic deposits were only covered by the Upper Lava Flows Succession, which has a maximum thickness of 70 m. The original load above these units may have been at least that of a 70 m lava pile (and the degraded unpreserved lava pile), a load that we will consider intermediate (in relation to the other units of the complex). Based only on the intruded units, we have no constraint to account if these dykes were intruded before or after the intense degradation episode.

Finally, the Root Complex plugs and necks of the original feeding system of the volcano are also intruded by numerous dykes. Again, from field data it is not possible to know if these dykes were intruded before the degradation (in which case they intruded at relatively large depths and may have been subjected to a load equivalent to a pile of ca. 1200 m) or intruded after intense degradation (in which case the load above them might have been negligible), or again if both cases are valid.

With the current state of knowledge of the volcano, too many assumptions may be needed to consider the emplacement depths and/or the load to which the dykes were subjected. Only dykes intruding the Cerro Bayo Breccia are undoubtedly near surface dykes.

Based on the geochemistry of dykes we tried to identify different groups that may indicate temporal or spatial occurrences. A general sketch of the position and units intruded by dykes for which we have whole-rock geochemical data is presented in Fig. 4 of the main text. Dykes have a basaltic trachy-andesites to (trachy)-andesites composition and one sample has dacitic composition (see Fig. 4 b). The Ba/Th vs. Eu/Eu\* diagram shows three different groups (A, B and C) with characteristic geochemical signatures (see Fig. 4 c). Figs. 4 d-f show the rare earth element (REE) patterns for samples of the different groups normalized to chondrite (Mc Donough and Sun, 1995). These diagrams indicate the typical signature of each group, but also testify small compositional variations given the parallel patterns of chondrite normalised REE diagrams but with variable absolute concentrations of REE within samples of each group that may be explained by simple processes such as different crystallization degrees.

From a geochemical point of view, there are at least 3 groups of dykes with characteristic signatures (see Figure 4). Given their signature and the intruded units, only dykes of Group C may have been subjected to a much higher load than the one currently observed. This inference is based on:

- a) groups A and B intrude the Cerro Bayo Breccia. This unit inferred to have been formed after the main degradation of the VPVC that produced the central depression (Guzmán et al., 2017).

Therefore, dykes intruding this unit may have suffered slight erosion during the arid climate that characterises the Puna during the last 6 Ma. Being of the same geochemical groups, although they also intrude the Nacimientos Breccia, the Root Complex and the undifferentiated epiclastic/volcanic deposits these dykes were intruded after the most important erosion of the complex, thus their currently observed exposure is considered similar to the original one.

b) group C intrudes undifferentiated epiclastic/volcanic material (covered by the 70 m-thick pile of lava flows) and the Root Complex. This unit was probably emplaced at a certain depth (not near surface). Based on all this information it is difficult to envisage that the differences in attitude and thickness observed at the VPVC are related to different emplacement depths or to differences in the local stress fields. We cannot however totally rule out this hypothesis. That’s why we have left the discussion open in this regard. Moreover, the different geochemical groups may indicate different contemporaneous magma chambers and/or relative age differences.

Table 2. Whole-rock geochemical analyses

Sample	VP1	VP6	VP8	VP14	CJA02	VP28	VP20	VP5*	VP31
Intruded unit	Nacimientos Breccia	Root Complex	Root Complex	Undiff.	Undiff.	Co. Bayo Breccia	Co. Bayo Breccia	Root Complex	Co. Bayo Breccia
SiO <sub>2</sub>	51.26	50.59	55.22	58.21	52.19	55.4	51.5	60.62	65.1
Al <sub>2</sub> O <sub>3</sub>	16.26	15.92	16.73	16.48	15.85	16.46	17.71	18.26	15.55
Fe <sub>2</sub> O <sub>3</sub>	9.41	10.69	7.75	6.94	9.64	7.43	10.06	0.45	5.28
FeO								5.05	
MgO	3.91	4.99	3.82	2.14	4.38	2.52	3.30	0.60	0.89
CaO	7.60	7.10	5.97	5.14	7.56	4.91	7.21	5.40	4.24
Na <sub>2</sub> O	2.80	2.86	2.99	2.55	2.67	3.46	3.35	3.18	2.65
K <sub>2</sub> O	3.36	3.74	2.79	3.66	3.27	3.41	3.57	3.30	3.52
TiO <sub>2</sub>	1.52	1.57	1.06	0.94	1.38	1.06	1.54	1.246	0.72
P <sub>2</sub> O <sub>5</sub>	0.63	0.83	0.36	0.31	0.55	0.35	1.06	0.324	0.37
MnO	0.16	0.17	0.15	0.09	0.13	0.15	0.19	0.036	0.09
Cr <sub>2</sub> O <sub>3</sub>	0.0048	0.0096	0.0027		0.0089	0.0014	0.0048	0.0014	0.000
LOI	2.8	1.2	2.9	3.3	2.1	5.15	1.19	1.68	1.81
Total	99.71	99.66	99.75	99.79	99.72	100.34	100.70	98.02	100.28
Ba	456	518	537	545	456	491	395	574	611
Be	2	2		2	2		2		1
Co	28.2	34.6	19.4	14.0	26.9	11.8	18.9		5.5
Cs	1.6	4.5	0.7	0.8	1.7	0.5	4.8	1.13	1.3
Ga	19.2	18.8	18.1	18.7	20.3	17.5	19.3	21	17.3

Hf	7.5	8.6	4.3	4.3	7.1	5.1	8.5	5.55	5.3
Nb	25.5	30.0	15.8	15.4	20.2	14.4	31.5	23.70	18.6
Rb	114.7	152.7	76.7	82.3	118.4	89.6	146.6	104.2	105.3
Sn	2	2		2	2	3	2		
Sr	530.8	537.4	575.4	542.8	507.0	481.6	531.8	580	436.4
Ta	1.4	1.8	0.9	1.0	1.3	0.8	1.9	1.69	1.1
Th	15.5	20.2	8.7	7.2	14.0	9.1	15.5	9.76	10.9
U	3.1	3.6	1.4	1.4	2.7	1.2	3.8	1.64	1.2
V	246	241	170	150	242	129	144	165	51
W	1.2	1.6	0.9	0.9	1.4	0.7	1.3		1.2
Zr	276.6	307.4	162.8	147.9	248.8	178.2	344.6	212	193.7
Y	33.9	34.4	23.9	21.2	32.0	26.1	39.2	30.12	25.1
La	44.5	50.2	32.4	27.3	41.4	33.3	52.5	40.57	41.3
Ce	92.2	107.2	64.1	55.7	85.8	67.9	106.7	77.71	80.1
Pr	11.24	12.62	7.60	6.45	10.39	7.99	13.47	9.34	9.26
Nd	44.3	49.3	29.9	24.1	41.8	30.3	52.6	35.61	35.8
Sm	8.80	9.54	5.75	4.81	8.11	6.67	10.61	7.30	6.79
Eu	1.89	2.02	1.48	1.37	1.81	1.54	2.14	2.03	1.46
Gd	7.75	7.85	5.17	4.52	7.32	5.59	9.33	6.49	5.74
Tb	1.15	1.21	0.80	0.72	1.12	0.87	1.38	1.01	0.83
Dy	6.12	6.38	4.28	3.75	5.79	4.91	7.49	5.93	4.07
Ho	1.20	1.28	0.84	0.79	1.15	0.87	1.47	1.18	0.99
Er	3.30	3.41	2.41	2.17	3.33	2.80	3.96	3.07	2.59
Tm	0.47	0.50	0.34	0.31	0.47	0.41	0.61	0.45	0.40
Yb	3.22	3.34	2.28	2.05	2.99	2.58	3.99	2.78	2.46
Lu	0.45	0.49	0.34	0.31	0.46	0.42	0.57	0.43	0.38

Methodology for whole-rock geochemistry

All samples except VP5 were analysed at ACME Labs (Vancouver, Canada). Samples were crushed, split and pulverized to a grain size lower than 200 mesh and fused in a platinum–gold crucible with a commercial lithium tetraborate flux. The molten material was cast in a platinum mold obtaining fused discs that were analysed by XRF. Natural rocks of known composition and pure quartz reagent (blank) were used as reference standards. The analytical accuracy was controlled using the geological standard material STD SO-18 and STD SY-4(D) which represent similar materials; based on replicate analyses the estimated uncertainties for major element measurements are < 0.04 wt. % for all elements. Detection limits are between 0.1 and 0.01%.

At the Washington State University laboratory (Seattle, USA), sample VP5 was analysed with a ThermoARL Advant'XP+ sequential X-ray fluorescence (XRF) spectrometer. Samples were crushed, split and pulverized using an agate mill at the Universidad Nacional de Cordoba, Argentina. This rock powder was analysed at the Washington State University lab with a di-lithium tetraborate flux (2:1 flux:rock) to produce fused beads, fusing at 1000°C in a muffle oven, and cooling; the bead was then reground, refused and polished on diamond laps. Natural rocks of known composition and pure quartz reagent (blank) were used as reference standards (USGS standard samples using the values recommended by Govindaraju, 1994). Details on the procedure are given in Johnson et al. (1999).

## Supplementary file 2.

### Numerical simulations of cooling dykes

#### *Theory and equations*

The internal temperature distribution of a magma chamber is calculated using the Finite Element (FE) method, by solving the heat transfer equation, assuming as negligible the effect of viscous heating and pressure-volume work:

$$\rho C_p \frac{\partial T}{\partial t} + \rho C_p \mathbf{u} \cdot \nabla T = \nabla(k \nabla T) + \mathbf{Q} \quad (1)$$

where the equation parameters refer to density ( $\rho$ ), specific heat capacity at constant pressure ( $C_p$ ), temperature ( $T$ ), time ( $t$ ), the velocity vector ( $\mathbf{u}$ ), thermal conductivity ( $k$ ) and  $\mathbf{Q}$  contains heat sources other than viscous heating (see Table S2.1 for more details concerning thermal and physical parameters). Since we are dealing here with pure conductive heat transfer (i.e.  $\mathbf{u}=0$ ), Equation (1) can be rearranged as follows:

$$\rho C_p \frac{\partial T}{\partial t} + \nabla(-k \nabla T) = \mathbf{Q} \quad (2)$$

The geometric modelling, mesh discretization and numerical computations were carried out with the COMSOL Multiphysics v5.2a software package (<http://www.comsol.com>). To simulate the solidifying magma, we use the *heat transfer with phase change* module. The latter allows solving the heat equation after setting the properties of a phase-change material (from liquid to solid) according to the Apparent Heat Capacity formulation (AHC) (Canot et al., 2009; Hu and Argyropoulos, 1996; Voller et al., 1990). The reader is referred to the work by Rodriguez et al. 2015 for more details on the methodology.



Table S2.1: Physical and thermal parameters used in the numerical simulations

Symbol	Value	Variable	SI Unit
$Cp_{crust}$	$342 + 1.774 T^* - 1.25 \times 10^{-3} T^{*2} + 3.2 \times 10^{-7} T^{*3}$	Specific heat capacity of crust <sup>[1]</sup>	J/kg°C
$Cp_{melt}$	Table S2.2	Specific heat capacity of magma (melt phase)	J/kg°C
$Cp_{solid}$	Table S2.2	Specific heat capacity of magma (solid phase)	J/kg°C
$h$	150	Dyke length	m
$\kappa_{magma}$	$f(T)^{[2]}$	Magma thermal diffusivity <sup>[2]</sup>	m <sup>2</sup> /s
$\kappa_{crust}$	$f(T)^{[2]}$	Crust thermal diffusivity <sup>[2]</sup>	m <sup>2</sup> /s
$k_{magma}$	$k_{magma} = \kappa_{magma} \rho_{magma} Cp_{magma}$	Magma thermal conductivity <sup>[2]</sup>	W/m°C
$k_{crust}$	$k_{crust} = \kappa_{crust} \rho_{crust} Cp_{crust}$	Crust thermal conductivity <sup>[2]</sup>	W/m°C
$L$	400	Latent heat of crystallization <sup>[1]</sup>	kJ/kg
$\phi$	Table S2.2	Melt fraction <sup>[3]</sup>	-
$\rho_{crust}$	2800	Crust density	kg/m <sup>3</sup>
$\rho_{magma}$	2500	Magma density	kg/m <sup>3</sup>
$\theta$	1- $\phi$	Solid fraction <sup>[3]</sup>	-
$thermal\_grad$	30	Crustal thermal gradient	°C/km
$T_{liquidus}$	1159	Magma liquidus temperature <sup>[3]</sup>	°C
$T_{solidus}$	840	Magma solidus temperature <sup>[3]</sup>	°C
$T_{surface}$	20	Surface temperature	°C
$w$	1,3	Dyke width	m

[1] Bea (2010); [2] Whittington et al. (2009); [3] use rhyolite-MELTS code 1.0.2 by Gualda et al. (2012).

The FE 2-D models are constructed over a Cartesian coordinate system with positive  $y$  values related to altitudes above sea level (Fig. S2.1). The computational domain corresponds to a 1 km wide section of the

crust stretching to a depth of 1 km under the sea level (Fig. S2.1a). The FE mesh consists of around 300,000 linear triangular elements, with up to 50m in size at the host rock and 2.5 and 8 cm at the dyke margins and interior, respectively (Fig. S2.1b).

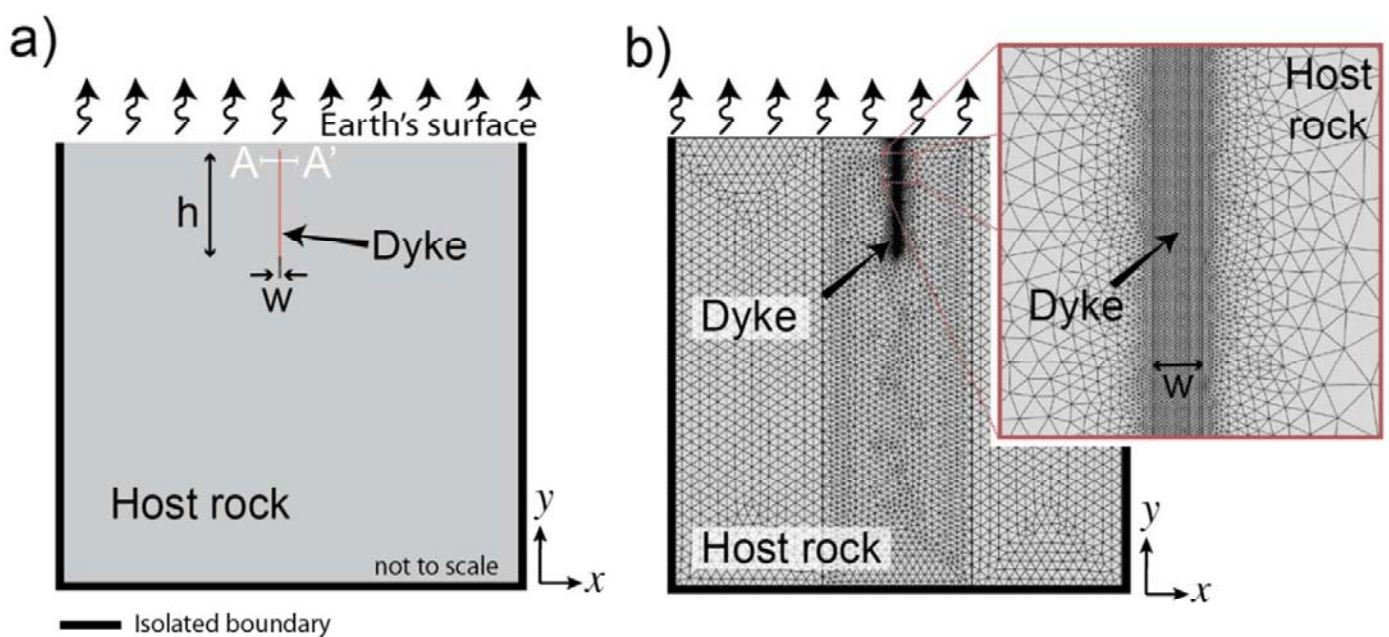


Fig. S2.1: (a) Sketch of the numerical models set-up also showing the boundary conditions used. The cross section A-A' runs at 20m depth (b) Example of the Finite Element mesh used for the modelling.

#### Physical and thermal properties and boundary conditions

For the sake of simplicity of the models, we assume that the dyke is instantly filled before solidification starts. It is considered that the magma is emplaced as entirely liquid. The melt ( $\phi$ ) and solid ( $\phi$ ) fractions of the crystallizing magma (composition equivalent to the CJA02 dyke, i.e., our example of a pulsating dyke) are determined by simulations conducted with the rhyolite-MELTS v1.0.2 code (Gualda et al., 2012), which replaces the old MELTS model (Ghiorso and Sack, 1995). Results obtained are reported in Table S2.2 and serve as input data for the heat transfer simulation with COMSOL Mutliphysics. We simulate an isobaric cooling at 250bar pressure (< 1km below surface), and redox conditions one log unit above the nickel-nickel oxide (NNO). The thermal properties of the crust and magma are obtained as described by Rodriguez et al. (2015) and final values are listed in Table S2.2. The initial temperature of the magma (1159°C) was estimated by using the geothermometer of plagioclase-liquid equilibria (Putirka, 2008) of sample CJA-02.

The initial temperature profile for the country rock is defined according to the geothermal gradient fixed at 30 °C/km typical of the continental crust at the Andes (e.g., Morgan, 1984) and assuming thermal conditions similar to those of Bea (2010). Heat flux is zero through the lateral walls of the country rock (i.e. isolating walls). For the dyke, we assume an initial temperature equivalent to the liquidus temperature provided by rhyolite-MELTS v1.0.2 (Gualda et al., 2012) (1159 °C assuming 0 wt% H2O due to total loss of volatiles at very low pressures as those found near the surface).

Table S2.2 Melt and solid fraction with temperature for the selected example. Specific heat capacity at constant pressure for the magma, as well as the melt and solid phases are also indicated.

T (°C)	Melt fraction	Solid fraction	$Cp_{melt}$ (J/kgK)	$Cp_{solid}$ (J/kgK)	$Cp_{magma}$ (J/kgK)
1159	0.99	0.00	1421.80	970.14	1410.65
1149.77	0.99	0.00	1421.74	968.72	1410.53
1144.77	0.99	0.00	1421.68	967.31	1410.39
1139.77	0.99	0.00	1421.41	1082.41	1409.87
1134.77	0.99	0.01	1420.39	1156.45	1408.03
1129.77	0.98	0.01	1419.41	1164.78	1406.18
1124.77	0.98	0.01	1418.46	1163.95	1404.29
1119.77	0.98	0.02	1417.55	1158.89	1402.33
1114.77	0.96	0.03	1415.84	1148.15	1396.19
1109.77	0.93	0.06	1413.52	1144.50	1386.38
1104.77	0.89	0.10	1410.46	1148.44	1373.38
1099.77	0.85	0.14	1407.59	1149.69	1361.43
1094.77	0.82	0.18	1404.90	1150.56	1350.68
1089.77	0.79	0.21	1402.38	1151.33	1341.02
1084.77	0.76	0.24	1400.00	1152.04	1332.29
1079.77	0.73	0.26	1397.76	1152.68	1324.36
1074.77	0.71	0.29	1395.63	1153.27	1317.11
1069.77	0.68	0.31	1393.62	1153.80	1310.45
1064.77	0.66	0.33	1391.71	1154.26	1304.30
1059.77	0.64	0.35	1389.89	1154.68	1298.60
1054.77	0.62	0.37	1388.35	1155.69	1293.22
1049.77	0.60	0.39	1387.06	1157.11	1288.16
1044.77	0.58	0.41	1385.81	1158.23	1283.49
1039.77	0.56	0.43	1384.61	1159.12	1279.16
1034.77	0.55	0.45	1383.43	1159.82	1275.12
1029.77	0.53	0.46	1382.30	1160.36	1271.34

1024.77	0.52	0.48	1381.01	1160.53	1267.73
1019.77	0.50	0.49	1379.75	1160.60	1264.31
1014.77	0.49	0.50	1378.54	1163.96	1262.74
1009.77	0.48	0.51	1377.39	1164.02	1259.75
1004.77	0.47	0.52	1376.28	1164.05	1256.90
999.77	0.46	0.54	1375.22	1164.04	1254.19
994.77	0.45	0.55	1374.20	1164.00	1251.61
989.77	0.44	0.55	1373.22	1163.92	1249.14
984.77	0.43	0.56	1372.28	1163.81	1246.78
979.77	0.42	0.57	1370.89	1163.69	1244.18
974.77	0.41	0.58	1369.43	1163.54	1241.63
969.77	0.40	0.59	1367.57	1163.80	1238.76
964.77	0.39	0.61	1365.46	1164.27	1235.75
959.77	0.38	0.62	1363.43	1164.65	1232.92
954.77	0.37	0.63	1361.47	1164.95	1230.23
949.77	0.36	0.64	1359.58	1165.16	1227.68
944.77	0.35	0.65	1357.75	1165.31	1225.26
939.77	0.34	0.66	1355.99	1165.39	1222.95
934.77	0.33	0.66	1354.29	1165.41	1220.73
929.77	0.32	0.67	1352.65	1165.39	1218.61
924.77	0.29	0.70	1350.59	1166.32	1212.63
919.77	0.26	0.73	1348.59	1166.90	1207.52
914.77	0.24	0.75	1346.66	1167.21	1203.23
909.77	0.22	0.77	1344.80	1167.35	1199.55
904.77	0.20	0.80	1342.06	1167.77	1194.45
899.77	0.18	0.81	1339.96	1167.79	1191.13
894.77	0.17	0.83	1337.93	1167.73	1188.17
889.77	0.15	0.84	1335.95	1167.60	1185.51
884.77	0.14	0.85	1334.01	1167.42	1183.09
879.77	0.13	0.86	1332.11	1167.21	1180.86
874.77	0.12	0.87	1330.25	1166.97	1178.79
869.77	0.11	0.88	1328.43	1166.71	1176.85
864.77	0.11	0.89	1326.64	1166.42	1175.04
859.77	0.10	0.90	1324.88	1166.13	1173.32
854.77	0.09	0.90	1323.15	1165.82	1171.68
849.77	0.08	0.91	1321.44	1165.50	1170.13
844.77	0.08	0.91	1319.76	1165.18	1168.63
839.77	0.07	0.92	1318.11	1164.86	1167.20
834.77	0.07	0.93	1316.47	1164.53	1165.82
829.77	0.04	0.95	1315.27	1164.57	1162.14

639.77                      0.01                      0.98                      1846.83                      1173.25                      1172.47

Results

Results obtained indicate how for a 1 m wide dyke (considering even a wider dyke than the one found at our field example, i.e. brecciated domain of dyke 33 at Table S1.1), temperatures at the interior of the dyke are below solidus - and hence able to **become** fragmented- (< 840 °C) after 4.6 days. Contrarily, e.g., it takes over a month to cool the interior of a 3 m wide dyke below the solidus temperature.

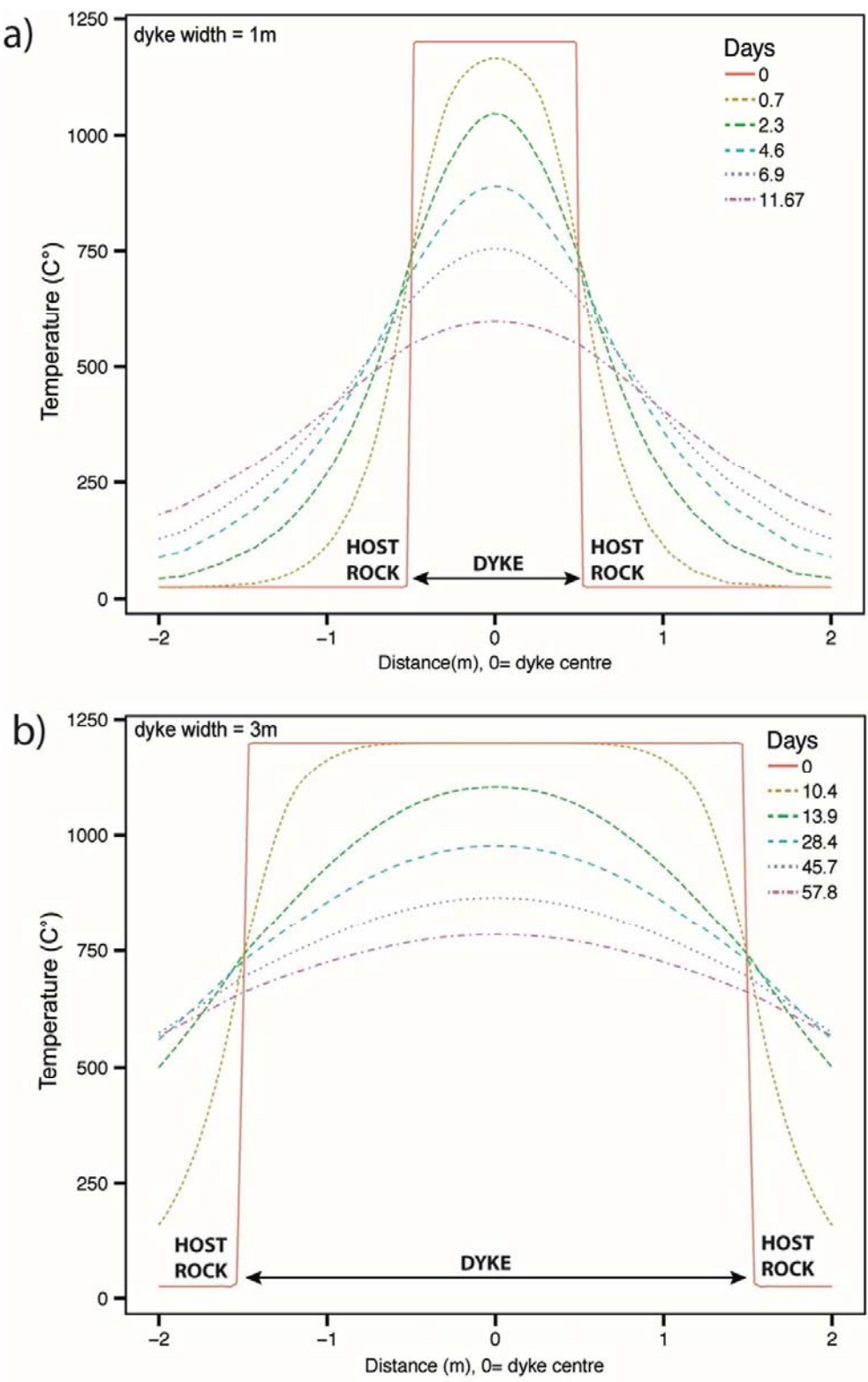


Figure S2.2: Temperature profile along the A-A' cross section (i.e. 20m depth) for the 1m (a) and 3m (b) wide dykes.

#### References

- Bea, F., 2010. Crystallization Dynamics of Granite Magma Chambers in the Absence of Regional Stress: Multiphysics Modeling with Natural Examples. *Journal of Petrology*, **51**(7), 1541-1569. doi:10.1093/petrology/egq028
- Canot, E., March, E. and Muhieddine, M., 2009. Various Approaches for Solving Problems in Heat Conduction with Phase Change. *International Journal on Finite Volumes*, **6**(1), 1-20.
- Ghiorso, M.S. and Sack, R.O., 1995. Chemical mass transfer in magmatic processes IV. A revised and internally consistent thermodynamic model for the interpolation and extrapolation of liquid-solid equilibria in magmatic systems at elevated temperatures and pressures. *Contributions to Mineralogy and Petrology*, **119**(2), 197-212. <http://dx.doi.org/10.1007/bf00307281>.
- Gualda, G. A. R., Ghiorso, M. S., Lemons, R. V., and Carley, T. L., 2012. Rhyolite-MELTS: a Modified Calibration of MELTS Optimized for Silica-rich, Fluid-bearing Magmatic Systems. *Journal of Petrology*. doi:10.1093/petrology/egr080
- Hu, H. and Argyropoulos, S.A., 1996. Mathematical modelling of solidification and melting: a review. *Modelling and Simulation in Materials Science and Engineering*, **4**(4), 371.
- Morgan, P., 1984. The thermal structure and thermal evolution of the continental lithosphere, in Pollack, H.N., ed. Structure and evolution of the continental lithosphere. *Physics and Chemistry of the Earth*, **15**, 107-193.
- Putirka, K., 2008. Thermometers and Barometers for Volcanic Systems. In: Putirka, K., Tepley, F. (Eds.), Minerals, Inclusions and Volcanic Processes, *Reviews in Mineralogy and Geochemistry*, Mineralogical Soc. Am., **69**, 61-120.
- Rodríguez, C., Geyer, A., Castro, A. and Villaseñor, A., 2015. Natural equivalents of thermal gradient experiments. *Journal of Volcanology and Geothermal Research*, **298**, 47-58. <http://dx.doi.org/10.1016/j.jvolgeores.2015.03.021>
- Voller, V.R., Swaminathan, C.R. and Thomas, B.G., 1990. Fixed grid techniques for phase change problems: A review. *International Journal for Numerical Methods in Engineering*, **30** (4), 875-898. doi: 10.1002/nme.1620300419
- Whittington, A. G., Hofmeister, A. M., Nabelek, P. I., 2009. Temperature-dependent thermal diffusivity of the Earth's crust and implications for magmatism. *Nature*, **458**(7236), 319-321. doi:10.1038/nature07818

## Supplementary file 2.

### Numerical simulations of cooling dykes

#### *Theory and equations*

The internal temperature distribution of a magma chamber is calculated using the Finite Element (FE) method, by solving the heat transfer equation, assuming as negligible the effect of viscous heating and pressure-volume work:

$$\rho C_p \frac{\partial T}{\partial t} + \rho C_p \mathbf{u} \cdot \nabla T = \nabla(k \nabla T) + \mathbf{Q} \quad (1)$$

where the equation parameters refer to density ( $\rho$ ), specific heat capacity at constant pressure ( $C_p$ ), temperature ( $T$ ), time ( $t$ ), the velocity vector ( $\mathbf{u}$ ), thermal conductivity ( $k$ ) and  $\mathbf{Q}$  contains heat sources other than viscous heating (see Table S2.1 for more details concerning thermal and physical parameters). Since we are dealing here with pure conductive heat transfer (i.e.  $\mathbf{u}=0$ ), Equation (1) can be rearranged as follows:

$$\rho C_p \frac{\partial T}{\partial t} + \nabla(-k \nabla T) = \mathbf{Q} \quad (2)$$

The geometric modelling, mesh discretization and numerical computations were carried out with the COMSOL Multiphysics v5.2a software package (<http://www.comsol.com>). To simulate the solidifying magma, we use the *heat transfer with phase change* module. The latter allows solving the heat equation after setting the properties of a phase-change material (from liquid to solid) according to the Apparent Heat Capacity formulation (AHC) (Canot et al., 2009; Hu and Argyropoulos, 1996; Voller et al., 1990). The reader is referred to the work by Rodriguez et al. 2015 for more details on the methodology.